Detailed Flow Investigations Within a High-Speed Centrifugal Compressor Impeller

D. ECKARDT

Research Engineer,
Institut fur Luftstrahlantriebe,
Cologne 90, West Germany

Detailed accurate measurements of velocities, directions, and fluctuation intensities were performed with a newly developed laser velocimeter in the internal flow field of a radial discharge impeller, running at tip speeds up to 400 m/s. Relative flow distributions are presented in five measurement areas from inducer inlet to impeller discharge. The impeller flow pattern, which coincides largely with potential-theory calculations in the axial inducer, becomes more and more reversed when the flow separates from the blade suction side, developing a rapidly increasing wake in the radial impeller. The observed secondary flow pattern and effects of channel curvature and system rotation on turbulence structure are discussed with respect to separation onset and jet/wake interaction.

Introduction

Remarkable progress has been made in the last years in advancing the performance of high-speed, high-pressure-ratio centrifugal compressor stages, but there is still a large potential for further improvements. The greatest prospect for advancement may be expected by superseding present methods of empirical correlation and extrapolation of existing stages with a design procedure which is largely supported by a physical understanding of real flow phenomena. The urgency to set up a theoretical framework for design optimization based on secure detailed flow measurements is additionally underlined by the fact that the complicated flow structure in radial fluid machines causes even the most sophisticated fluid dynamics theory to fail at present.

Up to now a great number of experimental investigations on centrifugal pumps, as well as on compressors, at relatively low speeds have already provided a qualitatively good survey of the flow field in centrifugal impellers. Here the publications of Fischer and Thoma [1],[1] Fujie [2], Senoo, et al. [3], Fowler [4], Howard and Kittmer [5], and Mizuki, et al. [6] have to be mentioned. If the knowledge of the essential internal flow phenomena at realistic conditions could be deepened, this would greatly enlarge the possibilities to develop a satisfactory analytical treatment, based on simplified, i.e. mathematically tractable but physically still relevant, flow models.

Opportunities for possible efficiency increases lie mainly in the flow diffusing elements. This enlightens the fact that advanced high-performance centrifugal compressors require the highest possible amount of flow diffusion, both in the rotor and in the adjoining vaned diffuser. Therefore a frequent occurrence in the second half of the relatively long impeller flow passages is a rapid growth of the boundary layers, which very often initiates flow separation from the blade suction side and the succeeding formation of a wake region, which shifts the through-flow (jet), in contrast to theoretical predictions, toward the blade pressure side. The flow separation impairs the diffusion potential and leads to a highly distorted jet/wake velocity pattern at impeller discharge, which causes a further reduction of stage efficiency due to mixing-losses and unsteady flow in the subsequent diffuser.

Consequently it is of primary interest to investigate the centrifugal impeller internal flow field at real operation conditions, especially the problems of separation onset and the subsequent jet/wake interaction. When a research program on high-speed, high-pressure-ratio centrifugal compressors was started at DFVLR, it was therefore decided to concentrate on the detailed study of the impeller flow pattern. The decisive precondition for the intended research program was the development of various dynamic measurement systems of high time- and space-resolution power, fitted for the extraordinary operating conditions. First a series of probe systems based on minature pressure transducers and hot-wire anemometry was developed. These measurements techniques were presented in [7]; results of instantaneous probe measurements in the jet/wake discharge flow of a high-speed centrifugal compressor impeller were given in [8].

In the meantime the successful development of a contactless operating laser velocimeter makes possible a direct analysis of the distorted flow field inside the impeller blade channels. This paper describes tests with this novel measuring technique and presents typical results of detailed flow investigations within a centrifugal compressor impeller, running at tip speeds up to 400 m/s.

The Test Rig

As our current research activities are mainly concerned with detailed investigations of impeller flow phenomena, a stage design with relatively large dimensions and with a vaneless diffuser was selected so that the impeller flow is not affected by downstream diffuser distortions.

[1]Numbers in brackets designate References at end of paper.

Contributed by the Fluids Engineering Division of THE AMERICAN SOCIETY OF MECHANICAL ENGINEERS and presented at the Gas Turbine and Fluids Engineering Conference, New Orleans, La., March 21–25, 1976. Manuscript received at ASME Headquarters, January 5, 1976. Paper No. 76-FE-13.

A meridional sketch of the centrifugal compressor test rig is shown in Fig. 1. The compressor is driven by a d-c motor with a maximum power input of 1500 kW; the impeller speed can be continuously varied up to 27,000 rpm, corresponding to a stage stagnation pressure ratio PR = 7. The rig is operated in an open circuit; air-flow enters the stage through a straight axial inlet pipe, where mass-flow is measured by means of a venturi nozzle. The unshrouded centrifugal impeller, Fig. 2, is milled out of a block of aluminum alloy and has 20 radially ending blades. The blade camber lines have an elliptic shape in cylindric sections, as shown on the bottom sketch of Fig. 1. The attached vaneless diffuser has constant flow area up to $R/R_2 = 2$; aft of the diffuser the air-flow is bent axially into an annular settling chamber from where the air leaves through a tangential discharge duct with adjoining throttling valve. An additional throttle ring was mounted near diffuser discharge, Fig. 1, in order to prevent the exit flow from disturbing the axisymmetric impeller flow pattern.

A detailed description of the test rig, including a complete compressor test map is given in [8]; the present paper pertains essentially to extensive impeller flow investigations at a test point near stage optimum — at $n = 14{,}000$ rpm and $\dot{m} = 5.31$ kg/s, a stagnation pressure ratio PR = 2.1, and an isentropic stage efficiency $\eta_{is} = 0{,}88$ were reached, both measured between station "0" and "4" (Fig. 1).

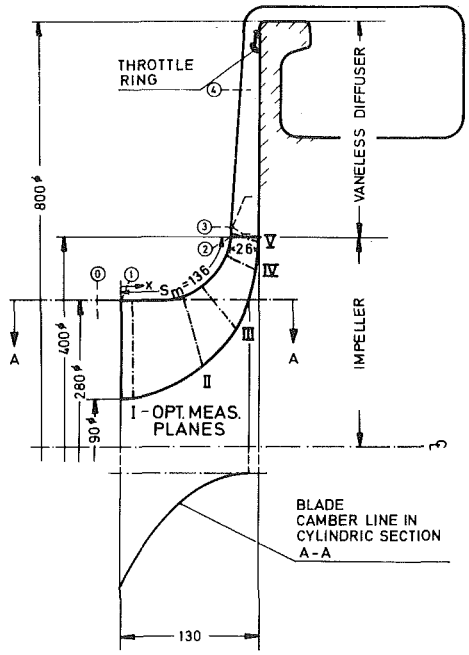

Fig. 1 Meridional cross-section of the centrifugal compressor stage with measurement location index, dimensions in mm

Nomenclature

A = area
b = meridional impeller channel width (Fig. 5)
c = absolute velocity (Fig. 5)
c_p = specific heat at constant pressure
f = relative fluctuation intensity (Fig. 4)
$f = \Delta c/(2\bar{c}) = (c_{max} - c_{min}) / (2\bar{c})$
L2F = Laser-2-Focus-Velocimeter
LDV = Laser-Doppler-Velocimeter
M = relative Mach number
$\dot{m}$ = mass flow rate
n = shaft speed
P = stagnation pressure
p = static pressure
PR = stagnation pressure ratio
PS = pressure side
q = absolute fluctuation intensity (Fig. 4)
$q = \Delta c/(2u_2) = (c_{max} - c_{min})/(2u_2)$
R = radius
R = gas constant
SS = suction side
s = entropy
s_m = meridional shroud contour length (Fig. 1)
T = stagnation temperature
t = static temperature
t,t' = blade spacing (Fig. 5)
u = impeller velocity (Fig. 5)
w = relative velocity (Fig. 5)
x = coordinate along meridional shroud contour (Fig. 1)
x/s_m = relative meridional shroud contour (Fig. 1)
y,y' = tangential coordinate beginning at blade pressure side (Fig. 5)
$y/t,y'/t'$ = relative blade spacing (Fig. 5)
z = coordinate normal to the shroud contour, beginning at casing wall (Fig. 5)
z_s = impeller tip clearance
z/b = relative meridional channel width (Fig. 5)
z_s/b_2 = relative impeller tip clearance
I, II, III, IV, V = optical measurement areas (Figs. 1 and 2)
α = absolute flow angle (Fig. 5)
β = relative flow angle (Fig. 5)
γ = relative velocity ratio
$\gamma = w_w/w_j$
Δc = absolute velocity fluctuation bandwidth (Fig. 4)
$\Delta c = c_{max} - c_{min}$
$\Delta\alpha$ = setting angle of the plane, containing the parallel laser beams, to a reference plane (Fig. 3)
$\Delta\beta$ = relative flow incidence to the blade surface
$\Delta\beta = \beta_{b,op} - \beta$
δ = pressure correction factor for standard conditions
$\delta = P/1.0133$ bar
ϵ = relative wake area
$\epsilon = A_w/A$
η = efficiency referred to stagnation conditions
Θ = temperature correction factor for standard conditions
$\Theta = T/288.1$ K

Subscripts

0,1,2,3,4 = stations in the stage (Fig. 1)
b = blade
is = isentropic
j = jet
m = meridional component
max = maximum
min = minimum
o = stagnation
op = optical, L2F-focal plane
rel = relative to impeller coordinates
S = standard condition
T = total, see definitions of $P_{T,rel}$ and $T_{T,rel}$
u = component in tangential coordinate direction y
w = wake

Superscripts

$\bar{}$ = statistically averaged (Fig. 4)
$\cdot$ = flow rate

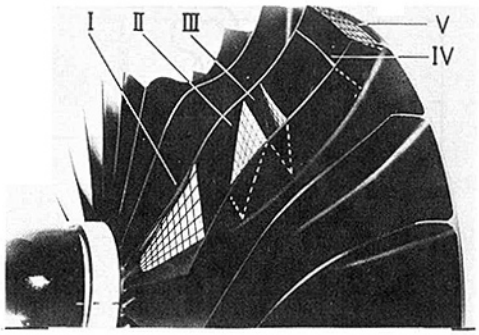

Fig. 2 Centrifugal compressor impeller with arrangement of optical measurement areas in the blade channel (impeller blackened by anodic treatment to reduce background radiation)

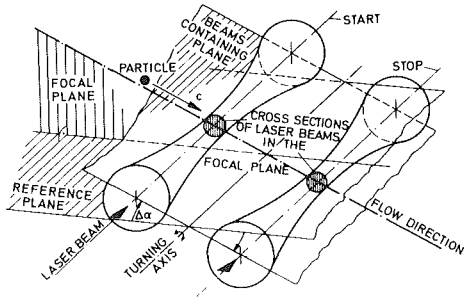

Fig. 3 Principle sketch of L2F measuring volume

Instrumentation

A new "Laser-2-Focus Velocimeter" (L2F), developed by Schodl, DFVLR, was applied successfully for the centrifugal compressor flow investigations. In principle this optical measurement technique has certain advantages, which make it especially suited for a detailed analysis of the high-turbulent flow field within the shallow blade channels of high-speed, high-pressure-ratio centrifugal compressor impellers.

The conditions in the L2F measuring volume are shown in Fig. 3. Similar to the Laser Doppler Velocimeter (LDV), the most established technique in this field, the L2F velocimeter measures the velocity of small light-scattering particles, which are additionally seeded into the fluid and follow the streamlines. The difference, however, lies in the fact that the LDV fringe pattern in the probe volume is replaced by two discrete, highly focused light beams, designated in Fig. 3 by "start" and "stop." This light-gate has–compared to LDV—a 100-times greater light concentration and creates a correspondingly high signal/noise ratio. This is advantageous in the used back-scatter operation mode, especially when the low signal intensity is superimposed by considerable background radiation due to laser light reflections in the vicinity of channel surfaces. As a result of focusing both beams have a converging/diverging cross section. The minimum beam-diameter is about 5–10 μm, the distance between the beams is fixed to about 0.5 mm, and the photo-optics detect particle-scattered light along the optical axis $\pm$ 1 mm off the focal plane. A particle passing both light beams in this range produces two successive pulses of scattered light; given the distance between the two laser beams, the measured time elapsed between the start/stop pulses yields the velocity of the flow perpendicular to the optical axis.

In order to register this double-pulse it is necessary, however, that the plane containing the start/stop laser beams is parallel to the flow direction; this can be achieved by rotating the L2F internal optics around the turning axis, Fig. 3. Consequently, it is possible to determine the flow direction relative to the known position of a reference plane.

In order to analyze high-turbulent flows adequately, it is

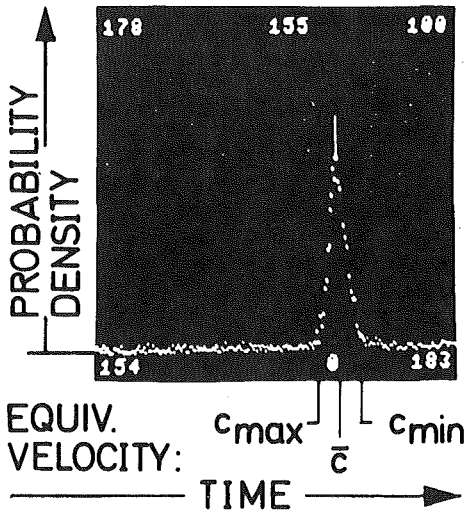

Fig. 4 L2F-output probability density distribution of particle passing-times between start/stop laser beams

expedient to adjust the setting angle $\Delta\alpha$, Fig. 3, in 8–10 angle steps around the presumed mean flow direction and to take up to 1000 measurements (start events) at each step. Signal processing is carried out with modern electronic equipment of sufficiently high time-response, operating in a start/stop mode. The collected data (stop events) are classified by means of a multi-channel-analyzer to probability density distributions, which are stored as a function of $\Delta\alpha$. Then the optimum of the enveloping curve of all probability density peaks corresponds to the most probable mean $\Delta\alpha$ within the observed flow direction spectrum.

Fig. 4 shows the probability density distribution for the optimum setting angle at a midchannel measurement position near the centrifugal impeller discharge. Along the abscissa the time is plotted which the particles need to pass the distance between both laser beams. The quantity of each time-measurement, corresponding to a distinct velocity in the turbulence spectrum, is arranged along the ordinate. The peak of that Gaussian bell-shaped distribution curve indicates the mean velocity $\bar{c}$, whereas the baseline width of the distribution illustrates the maximum occurring velocity fluctuation $\Delta c = c_{max} - c_{min}$.

In order to carry out measurements within the blade channels of turbomachine rotors, an opto-electronic trigger unit has been provided. The laser beam is interrupted—as directed by a blade trigger signal from the rotor—and released to a certain point in successive blade channels to take the measurements during 5 percent of the blade spacing t until enough data for an adequate statistical evaluation are gathered. More detailed information on the L2F technique is given by Schodl in [9,10].

In the present program the centrifugal impeller flow field was determined from inducer inlet to impeller discharge in five measuring areas, designated by I–V, the positions of which are illustrated in Figs. 1 and 2 and defined in Table 1.

Table 1 L2F measurement area locations

Area No.	x/s_m
I	0.08
II	0.43
III	0.59
IV	0.87
V	1.01

As illustrated in detail in Figs. 3, 4, and 5, the described L2F principle renders it possible to measure the amount $\bar{c}$, the direction $\bar{\alpha}$ of the statistically averaged absolute velocity vector and the fluctuation bandwith Δc in the laser focal plane. After calculating the local circumferential velocity u from impeller speed, geometry, and the relative width position z/b of the meas-

uring volume, the complete velocity triangle including relative velocity w and flow angle β can be determined.

Fig. 6 shows the centrifugal compressor test rig and the L2F velocimeter setup on the left. The laser beam passes through a cylindric casing window (5–20 mm dia depending on blade height), which is normally aligned to the shroud contour; to change the measuring position from hub to shroud the complete device is moved, whereas the circumferential position in the blade channel is determined by means of a time-delay unit combined with the aforementioned trigger-optics. Measurements down to about 2 mm off the four blade channel walls are possible.

With regard to the attainable L2F measurement accuracy the following statements have to be taken into account:

1 Measurement "points," as, e.g., those designated by circles in Figs. 7–11, actually indicate statistically averaged mean values of an oblique-angled prism-shaped measuring volume of 0.05 t circumferential length (0.75–3 mm), 2 mm width (along the laser axis), and max 0.5 mm height (beam distance).

2 The basic velocity uncertainty of the L2F velocimeter is for the determination of $\bar{c}$ in the range of $\pm$ 1 percent and for $\Delta c = c_{max} - c_{min}$ better than $\pm$ 3 percent. The flow angle resolution of this technique depends on the beam diameter-to-distance ratio and is for the presented setup better than $\pm$ 1 deg. These statements imply a measurement position of more than 4 mm off the flow channel walls and a fluctuation intensity $q = \Delta c/(2u_2) < 0.15$; the latter condition is maintained throughout the whole blade channel, except within the wake region.

3 In the wall zones, where the signal/noise ratio decreases, and within the excessively fluctuating region of separated flow, $q > 0.15$, it is difficult to determine a clear-cut optimum in the $\bar{c}$ and $\bar{\alpha}$ probability density distributions. Here, in extreme cases (e.g., wake wall zones), the estimated uncertainties will be up to $\bar{c}$ $\pm$ 5 percent, Δc $\pm$ 10 percent, and $\bar{\alpha}$ $\pm$ 5 deg.

4 The accuracy and operational usefulness of the L2F system became manifest by the excellent coincidence of the L2F measured velocity distribution at impeller discharge, Fig. 11, with results of instantaneous probe recordings of the distorted flow field in the diffuser entry region [8, 14]. A second overall accuracy check was performed by comparing a mass-flow balance of the L2F measurements in the different impeller measuring areas with the venturi-nozzle indication; the agreement of better than $\pm$ 4 percent appears to be very satisfactory with regard to the extremely difficult measuring conditions within the impeller flow field and the lack of measurement information in the immediate vicinity of the blade channel walls.

5 For statements on impeller speed and mass flow an accuracy of u_2 $\pm$ 0.03 percent and $\dot{m}$ $\pm$ 1.5 percent is claimed throughout this paper.

Experimental Results and Discussion

Figs. 7, 8, 9, 10, and 11 represent the continuous development of the flow distribution within the centrifugal impeller from inducer inlet (meas. area I) to impeller discharge (meas. area V) for the investigated test point $n/\sqrt{\Theta_0}$ = 14,000 rpm and $\dot{m} \cdot \sqrt{\Theta_0}/\delta_0$ = 5.31 kg/s (pressure and temperature correction factors δ_0 and Θ_0 referred to standard conditions $P_{0,S}$ = 1.0133 bar and $T_{0,S}$ = 288.1 K).

The perspective views show the locally measured meridional components of the absolute velocity c_m, Fig. 5, referred to the tip speed at impeller outlet u_2. In the diagrams the form of the measuring areas has been simplified to trapezium shapes at which the blade spacings and widths are equally scaled; the shroud-side casing wall lies in the front (z/b = 0), the hub in the rear (z/b = 1), and the hatched areas along the pressure side PS (y/t = 0) and suction side SS (y/t = 1) designate half of the blade thickness respectively.

A check of the relative flow pattern showed that the measured relative flow directions β coincide within $\pm$ 1 deg with the local blade angles $\beta_{b,op}$ of plane I. This indicates that the flow has already largely adjusted to the blade surface at this plane about 11 mm aft of impeller leading edge. Similar conclusions can be drawn from Fig. 8 for the conditions in the next measurement area II in the transition range from the axial inducer to the radial impeller. The flow is again very regular at a comparatively low blade loading and has still preserved its potential-theoretical character.

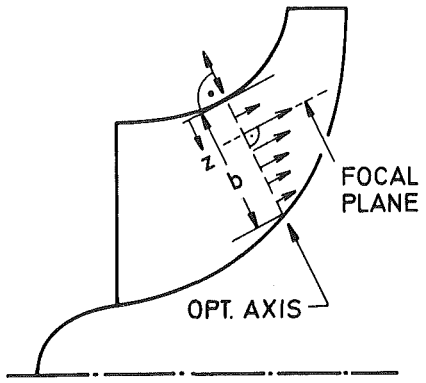

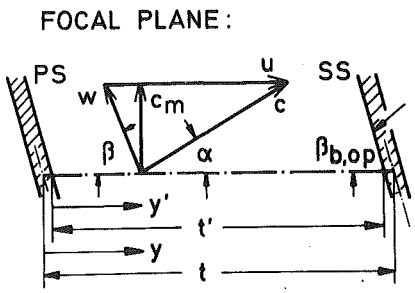

Fig. 5 Definition of L2F-measured and calculated velocity components in the impeller flow field

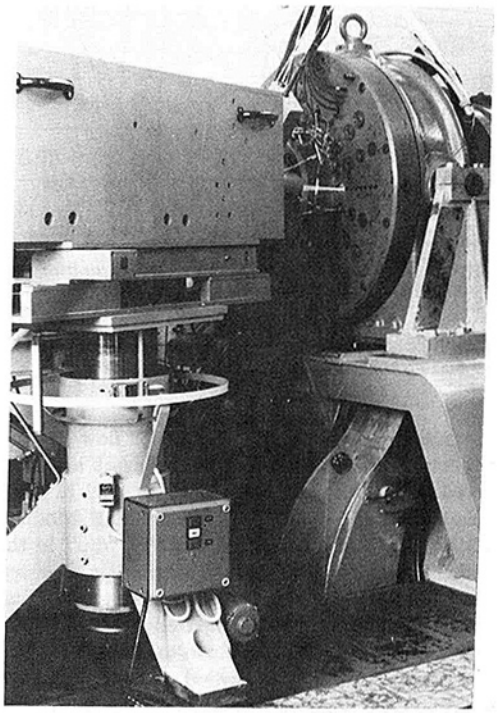

Fig. 6 Arrangement of the L2F velocimeter at centrifugal compressor test rig

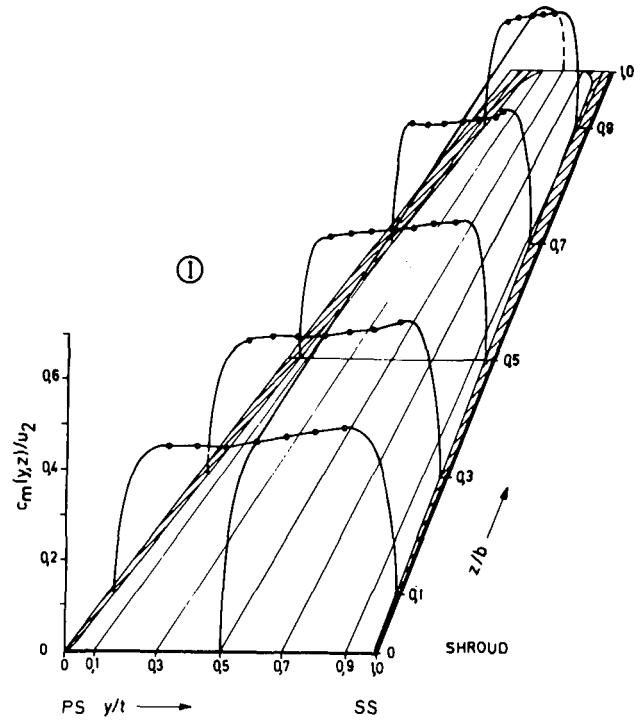

Fig. 7 Velocity distribution c_m/u_2 at measurement area I, n = 14,000 rpm, $\dot{m}$ = 5.31 kg/s, x/s_m = 0.08

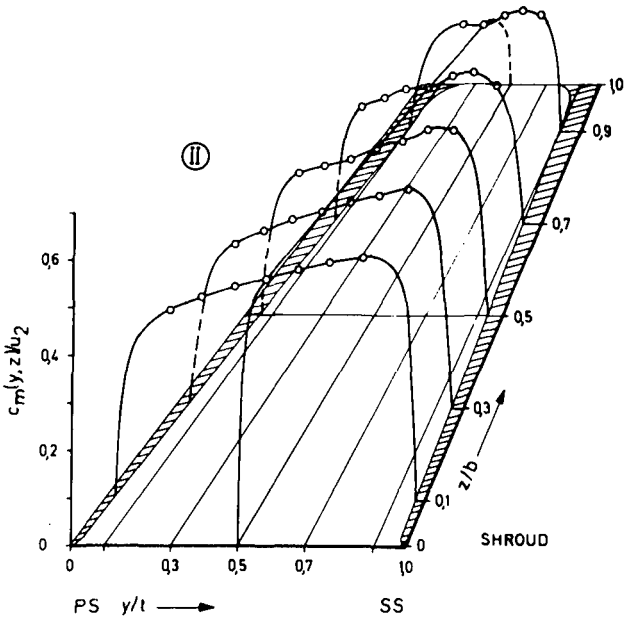

Fig. 8 Velocity distribution c_m/u_2 at measurement area II, n = 14,000 rpm, $\dot{m}$ = 5.31 kg/s, x/s_m = 0.43

First marked distortions of the impeller flow pattern appear a short distance downstream at measurement area III, as can be observed in Fig. 9. Here—at x/s_m = 0.59 in the range of highest blade loading (see also the corresponding shroud pressure maps, Fig. 7, in [8]—a pronounced velocity "dip" in the shroud stream-tube (z/b = 0.07) marks a beginning flow separation. In the rest of the blade channel the flow is preserving its theoretically predictable pattern, but compared to the foregoing measuring areas with a clearly steeper blade-to-blade velocity gradient. This is especially true of the shroud stream tube (y/t < 0.4) where additionally a distinct thickening of the casing wall boundary layer may be observed.

The beginning flow separation in measuring area III rapidly enlarges downstream, as shown in Figs. 10 and 11 for the subsequent areas IV and V, developing a pronounced wake. This wake area covers about 20 percent (IV), respectively 35 percent

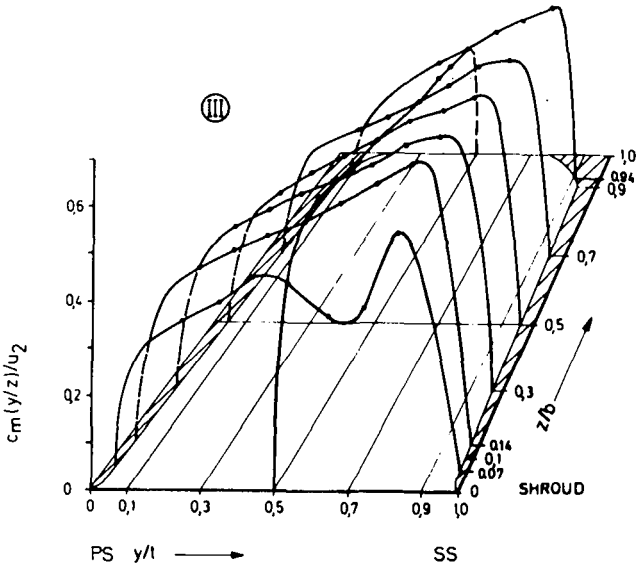

Fig. 9 Velocity distribution c_m/u_2 at measurement area III, n = 14,000 rpm, $\dot{m}$ = 5.31 kg/s, x/s_m = 0.59

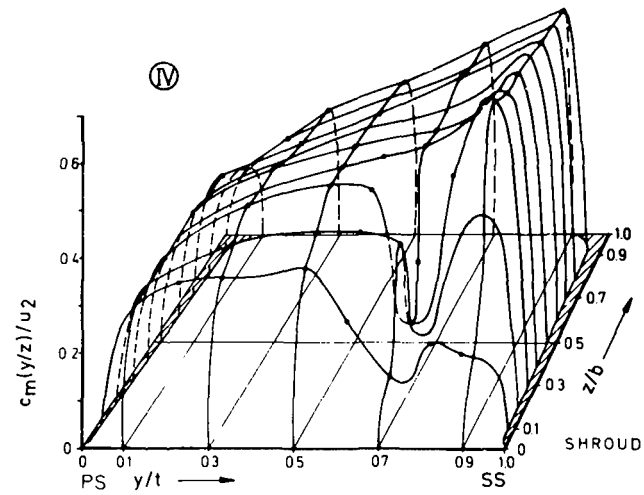

Fig. 10 Velocity distribution c_m/u_2 at measurement area IV, n = 14,000 rpm, $\dot{m}$ = 5.31 kg/s, x/s_m = 0.87

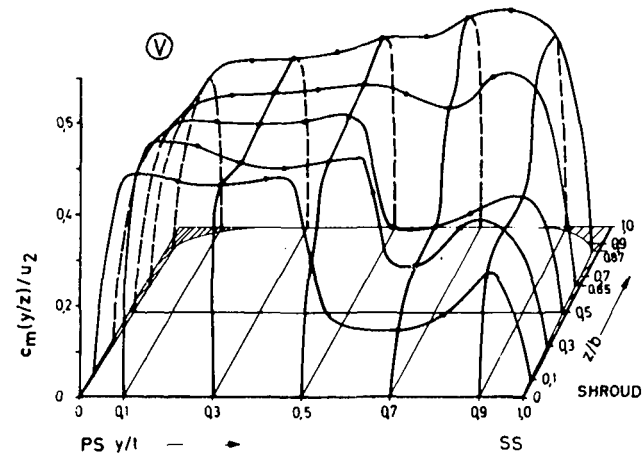

Fig. 11 Velocity distribution c_m/u_2 at measurement area V, n = 14,000 rpm, $\dot{m}$ = 5.31 kg/s, x/s_m = 1.01

(V) of the corresponding flow channel area. The wake region is characterized by

— a low mass-flow component, the wake comprises about 15 percent of the total mass-flow at impeller discharge,

— a high fluctuation[2] intensity, the local relative fluctuation intensity $f(y, z) = (c_{max} - c_{min})/(2\bar{c})$ reaches values of $f > 0.2$ in the wake area, whereas in the main flow $f = 0.05$–0.1 between area I and V,

— a steep, relatively stable velocity gradient to the surrounding main flow, this illustrates the separation of high- and low-energetic fluid material and the suppression of turbulent mixing along the jet/wake shear layer due to effects of the Coriolis force and meridional channel curvature, as predicted by Dean [11] and treated theoretically by Johnston in [12].

It is apparent from the velocity distribution, Fig. 10, that there is still, at least in the circumferential direction, a substantially potential-theoretical flow character. The thickening shroud wall boundary layer and the increasing displacement effect of the rapidly growing wake region initiate then a shift of the main flow toward the pressure side of the hub wall region.

Aft of the impeller the distorted flow pattern mixes out, but less rapidly than predicted by theoretical models with a "no-flow" assumption for the wake region [13]. As clearly demonstrated in our investigations on jet/wake mixing in the impeller exit/diffuser entry region [8, 14], the flow equalization process takes place mainly across the channel width due to decreasing meridional curvature turbulence stabilization, whereas the Coriolis forces maintain a remarkable circumferential flow distortion along the shroud wall up to $R/R_2 \approx 1.2$ (see also Fig. 15, where $\gamma = w_w/w_j$ represents the relative velocity distortion between wake w_w and jet w_j). The subsequent Figs. 12, 13, 14, and 15 are in comparison to the foregoing detailed plots rather aimed at an overall evaluation of the investigated impeller. E.g., Fig. 12 represents the total enthalpy development $c_u \cdot u/u_2^2$ within the impeller blade channels along five streamlines (see inset) from inducer inlet ($x/s_m = 0$) to impeller discharge ($x/s_m = 1$). This figure clearly demonstrates for $x/s_m < 0.6$ the present low-loaded inducer design and the tendency that within a measurement area—for $z/b = \text{const}$—the pressure side energy transfer exceeds that on the suction side and—for $y/t = \text{const}$—is higher near the shroud than at the hub.

Beyond $x/s_m \approx 0.6$ this tendency in circumferential direction is reversed due to strengthening secondary flows (see also Figs. 17 and 18); most striking is the rapid increase in the shroud/suction side (wake) stream-tube.

A comparison between L2F-measured velocity distributions and potential-theoretical flow calculations is carried out in Fig. 13, where relative velocity profiles w/u_2 are plotted for every measurement plane (I–V)—between shroud and hub at the

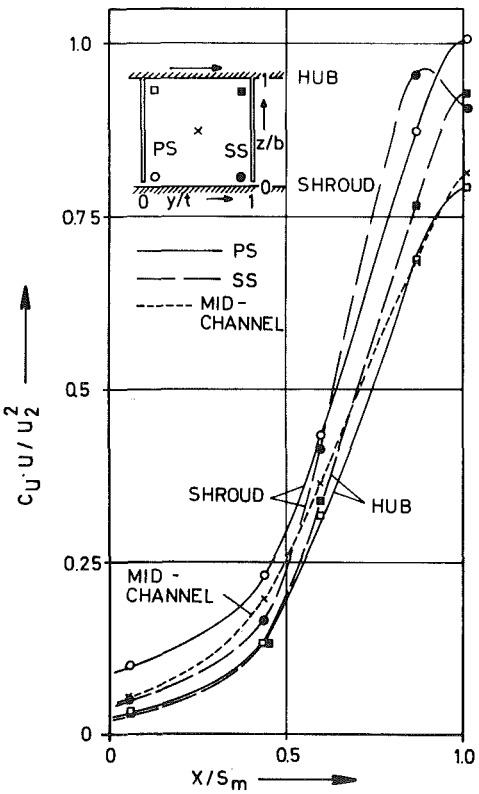

Fig. 12 Energy transfer within the impeller blade channels, n = 14,000 rpm, $\dot{m}$ = 5.31 kg/s

[2]In this context the term "fluctuation" comprises—due to the applied L2F measuring principle—local turbulence, unsteady relative flow (e.g., induced by recirculating wake flow, shifting separation onset, etc.), and, to a minor extent, pulsations in the overall mass flow (e.g., caused by slight imperfections in the axisymmetric diffuser flow field, which may occur despite of the inserted throttle ring, Fig. 1).

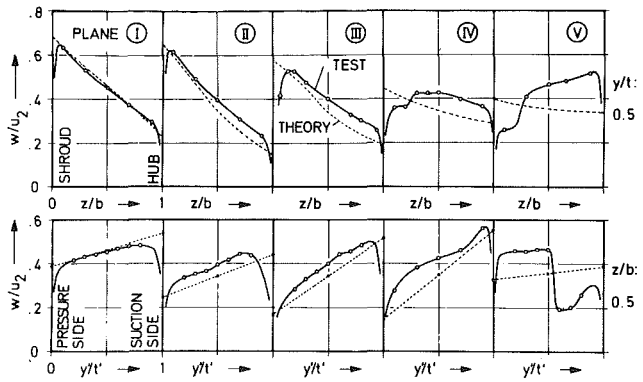

Fig. 13 Comparison of L2F relative velocity profiles w/u_2 with potential-theory calculations, n = 14,000 rpm, $\dot{m}$ = 5.31 kg/s

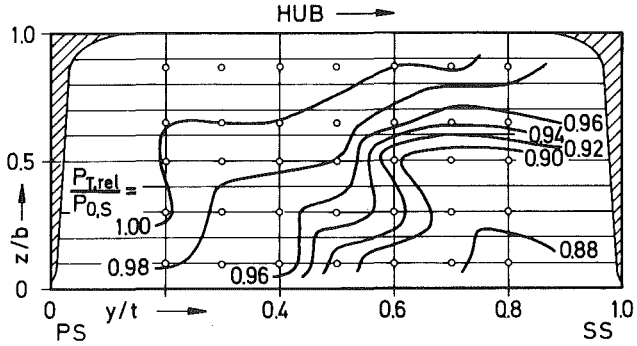

Fig. 14 Distribution of the pressure ratio $P_{T,rel}/P_{0,S}$ at centrifugal impeller discharge, measurement area V, n = 14,000 rpm, $\dot{m}$ = 5.31 kg/s, x/s_m = 1.01

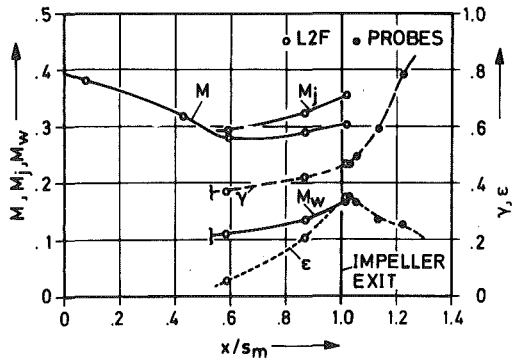

Fig. 15 Distributions of relative Mach numbers M, M_j, M_w, relative wake area ϵ, and relative velocity ratio γ along relative shroud contour x/s_m, n = 14,000 rpm, $\dot{m}$ = 5.31 kg/s

relative blade spacing $y/t = 0.5$ (upper row) and between pressure side and suction side at the relative blade with $z/b = 0.5$ (lower row).

The "test" shroud-to-hub profiles clearly show the actual flow diffusion with a pronounced gradient from plane II toward III, which results in a remarkable thickening of the shroud boundary layer in plane III, before the rapidly increasing wake region causes a displacement of the through-flow jet toward hub and pressure side. The circumferential distributions demonstrate again the high channel loading in the rear radial impeller (IV) and the sudden turnover (V) due to impeller discharge and wake development.

The potential-theoretical calculations were performed with a quasi-three-dimensional method. The shroud-to-hub solution is obtained with a streamline curvature method, based on the well-known papers of Stanitz, et al., e.g., [15]. The flow field is assumed to be axisymmetric up to 75 percent chord length from where impeller slip is considered. This solution is used to establish the location of the stream surfaces, whereas the "rapid approximate method" of Stanitz and Prian [16] yields the blade-to-blade solution on these stream surfaces.

The calculation results—projected into the laser focal plane—are in relatively good agreement with the test results in the low-loaded inducer and the radial impeller entry region; up to plane III the deviations of the test results from theoretical predictions may be explained partially by boundary layer displacement, before the rapidly developing wake region induces excessive deviations farther downstream. The same is valid for the blade-to-blade velocity gradient prediction, which fits the test results with satisfactory accuracy as long as no flow separation occurs.

Besides this comparison with potential-theory calculations the detailed L2F measurements offer the possibility to check and reevaluate existing, simplified models of the complicated centrifugal impeller flow. One of the most established flow models was suggested by Dean [17]:

The flow in the impeller passage consists essentially of a quiescent wake (statement 1) with negligible relative kinetic energy (2), adjacent to the suction surface (3), along with a nearly inviscid jet flow (4). Coriolis acceleration is assumed to suppress mixing between jet and wake (5), so that under these conditions it is deduced that the jet relative Mach number should remain constant aft of separation onset (6).

The foregoing discussion of the observed jet/wake pattern in the radial impeller enabled already some conclusions with regard to the statements (1, 2, 3, and 5) and—except (1)—confirmed these largely. Figs. 14 and 15 are intended to enlighten the background of statements (4, 6) on the inviscid, constant Mach number jet flow.

The loss analysis at impeller discharge is illustrated in Fig. 14 by the relative total pressure distribution $P_{T,\mathrm{rel}}$, referred to the inlet (standard) stagnation pressure $P_{0,S}$. Starting from the transformed energy equation

$$T_{T,\mathrm{rel}} = t + (w^2\text{-}u^2)/(2c_p) \tag{1}$$

and the assumption that there is no relative work (cover friction effects neglected) follows $T_{T,\mathrm{rel}} = T_{0,S}$ and consequently—with the relative velocity in the L2F measurement area V—the distribution of the static temperature $t(y,z)$. Now, the pressure loss $\Delta P_{T,\mathrm{rel}}$ defines $P_{T,\mathrm{rel}} = P_{0,S} - \Delta P_{T,\mathrm{rel}}$ so that $P_{T,\mathrm{rel}}$ is at the same entropy as the state in the measurement plane or—for isentropic flow—$P_{T,\mathrm{rel}} = P_{0,S}$. With the assumption that the instantaneous static pressure distribution p, measured at the shroud wall, is constant all over the measurement area V, follows the entropy distribution $s(y,z)$

$$s = c_p \ln(t/T_{0,S}) - R \ln (p/P_{0,S}) \tag{2}$$

and for the relative total pressure

$$P_{T,\mathrm{rel}} / P_{0,S} = e^{-s/R} \tag{3}$$

A more detailed derivation of $P_{T,\mathrm{rel}}$ is given by Dean, et al. in [18, Appendix VII].

Due to the implied simplifications the uncertainty for the $P_{T,\mathrm{rel}}$-distribution is estimated to be max ± 2 percent. Nevertheless the pronounced loss pattern in Fig. 14 clearly demonstrates that a flow model conception with the assumptions of an isentropic flow core in the jet and—in the wake—an accumulation of entropy generated within the impeller, due to passage and cover wall friction, tip leakage, and any other source, would be justified by and large for the present test point.

Fig. 15 shows the (area-mean) relative Mach number distributions M, M_j, and M_w (total-, jet- and wake-flow) along the relative meridional shroud contour x/s_m for the investigated test points. Upstream of the observed separation point $x/s_m \approx 0.55$ the flow diffuses rapidly, but then the diffusion stops abruptly at M = 0.29 and the jet is reaccelerated to $M_j = 0.35$ at impeller tip.

It has to be presumed that this difference compared with model statement (6) is closely related to an increased wake displacement effect, due to a wake mass flow, which is no longer negligible. Possibly a certain model refinement can be achieved in the future by considering this effect, which appears to be strongly interconnected again with the secondary flow pattern in the radial impeller (see also Fig. 17).

Additionally Fig. 15 contains the distributions of the relative velocity ratio $\gamma = w_w/w_j$ and the relative wake area $\epsilon = A_w/A$; both curves are extended into the vaneless diffuser entry region, based on instantaneous probe recordings [8, 14].

Analysis of Separation Onset and Jet/Wake Interaction

The importance of impeller flow diffusion on stage performance has been emphasized in the introduction. The decisive question in this context, which should be tackled by our experimental studies, is the evaluation of the relative importance of secondary flows and/or variations in the turbulence structure, due to system rotation and channel curvature, on separation onset and jet/wake interaction within the impeller.

A salient feature of the relative flow pattern, Fig. 16, is the general tendency of the core-flow toward the blade pressure side; this becomes especially evident in comparison with the blade surface angles in the optical plane $\beta_{b,\mathrm{op}}$, which are indicated along the suction side in Fig. 16. This lateral movement coincides with the flow deflection (slip) occurring in this part of the blade channel due to imperfect guiding of the fluid by the impeller blades. The cross-flow closes to a dominating main vortex in the shroud region (Fig. 17, arrow 1) which removes low-energy fluid material from the channel surfaces and feeds it into the wake. The same applies for a weaker secondary vortex in the region of hub wall and suction side (arrow 2). Additional low-energetic fluid material dumps through the tip clearance ($z_s/b_2 = 0.027$) into the wake region (arrow 3). The developing wake appears in this representation as a reservoir for low-energy fluid material coming from various sources.

The rapid increase of the wake between areas III and V (Figs. 9, 10, 11) suggests a certain interaction with the secondary flow intensity and, indeed, our measurement results indicate a comparable intensification of the cross-flow within the radial impeller. This is demonstrated in Fig. 18, where the secondary flows in the areas III and IV are compared, represented by the plotted $\Delta\beta$-distributions.

While blade-congruent flow is prevailing throughout the whole axial inducer, first weak secondary flows are preceptible in area III, where a thickened shroud boundary layer and indications of the beginning flow separation are observed. Losses, caused by both effects, are strengthening the total enthalpy gradient (primary vorticity) normal to the main flow direction, thus increasing also the induced (secondary) vorticity. Consequently, the observed secondary flow pattern confirms largely theoretical

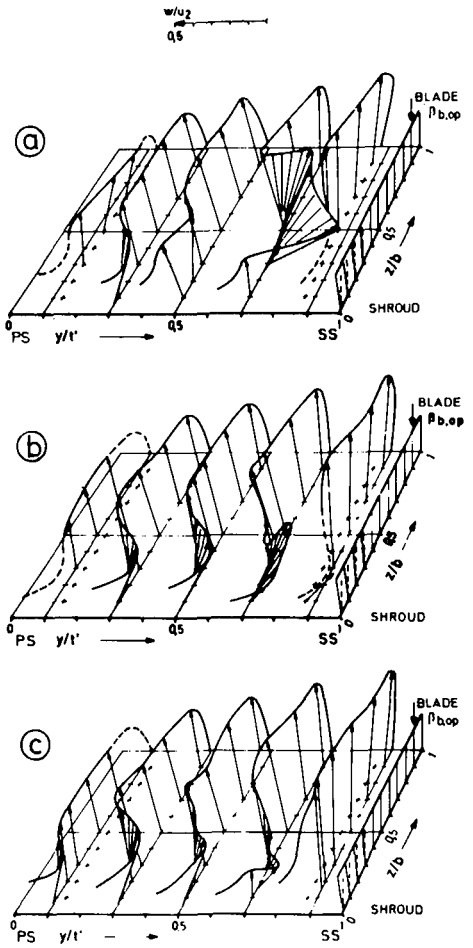

Fig. 16 Relative velocity distributions w/u_2 at measurement area IV (x/s_m = 0.87): (a) n = 18,000 rpm, $\dot{m}$ = 7.16 kg/s, (b) n = 14,000 rpm, $\dot{m}$ = 5.31 kg/s, (c) n = 10,000 rpm, $\dot{m}$ = 3.81 kg/s

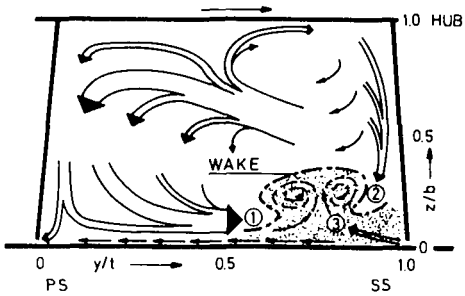

Fig. 17 Basic secondary flow pattern in the radial part of the centrifugal impeller (meas. area IV)

predictions, based on the theory of nonviscous flows with a total head gradient in the meridional plane (see, e.g., Kramer and Stanitz [19]).

The increasing secondary flow intensity additionally strengthened by the wake displacement supports the further feeding of low-energetic fluid into the wake, where system rotation and streamline curvature effects suppress the turbulent mixing between high- and low-energetic fluid material. The described mechanism explains the avalanche-type rapid increase of the wake area even in cases where the flow separates relatively far downstream in the impeller flow channels.

However, this does not allow any conclusion about the actual causes of the flow separation. To this end further detailed measurements are necessary, together with theoretical evaluations of the boundary layer development, as outlined by Bradshaw [20] and Eide and Johnston [21], and a considerable amount of fundamental research work like that of Moore [22] and Rothe and Johnston [23].

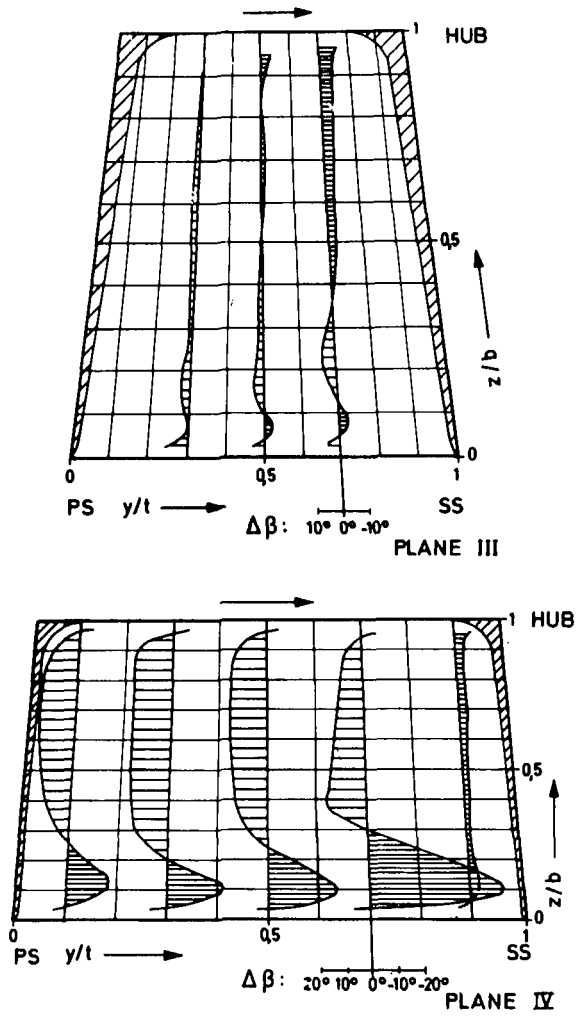

Fig. 18 Circumferentia' components of the impeller secondary flow pattern, represented in the form of $\Delta\beta$-distributions in the meas. areas III and IV ($\Delta\beta = \beta_{b,op} - \beta$, see Fig. 5)

There are only some hints and indications which support the assumption that in the present case the flow separation should mainly be initiated by curvature and rotational effects on turbulence structure (and then strengthened by following induced secondary flows):

1 The secondary flow intensity in measurement area III, which contains first indications of a beginning separation, is still relatively low, as illustrated in Fig. 18 (and negligible in the areas I and II).

2 The flow separation commences in the range of most extreme channel curvature (superposition of the meridional turning to radial and the elliptic blade shape).

3 There is actually a reduction of turbulence intensity immediately before the separation onset in the shroud/suction side corner.

The last statement is illustrated by measurement results in Fig. 19, where the absolute fluctuation intensity q in the shroud stream-tube is plotted along the relative meridional shroud contour x/s_m. In the definition $q = \Delta c/(2u_2)$, the difference of maximum and minimum absolute flow velocities Δc, observed in the fluctuation spectrum (Fig. 4), is referred to the impeller tip speed u_2. Most striking is the fluctuation development along the blade suction side:

After a steady increase of fluctuation intensity in the axial

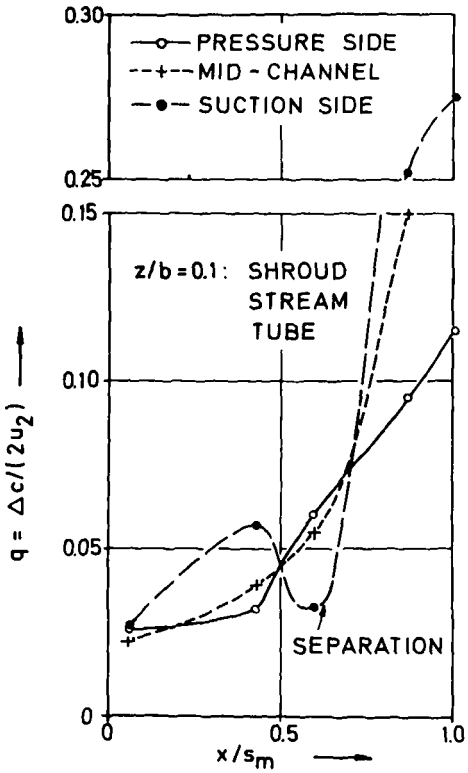

Fig. 19 Absolute fluctuation intensity q (along statistically averaged, absolute velocity vector c) at impeller shroud

inducer ($x/s_m < 0.5$), possibly caused by an accumulation of dumped tip clearance material, q is drastically reduced, corresponding to turbulence stabilization, when channel curvature and Coriolis forces become increasingly effective. Aft of the designated separation onset there is then a rapid fluctuation intensification in the highly pulsating wake region up to $q > 0.25$ at impeller discharge.

It has to be emphasized here that the preliminary conclusions, drawn from the presented data with regard to separation onset, are still restricted to the investigated impeller configuration (elliptic bladed impeller with radial discharge). Planned tests, at higher speeds, at different operation points, and with other impeller configurations (with backward-leaning blades and splitter-vanes in the radial part of the impellers), will help to establish a more generalized, secure figure of these important flow mechanisms in high-speed centrifugal compressor impellers.

Conclusions

1 Detailed investigations with the newly developed Laser-2-Focus Velocimeter revealed a largely potential-theoretical flow pattern up to the radial portion of the centrifugal impeller flow channels. From this it may be concluded that—provided one-dimensional design rules on energy transfer, mass flow rate, etc., were observed—potential-theoretical methods (possibly supplemented by boundary layer calculations) are fairly well suited to predict the undisturbed flow pattern within the axial inducer and, partially, the impeller.

2 In the investigated impeller first pronounced flow distortions appeared with increasing energy transfer at $x/s_m \approx 0.6$, indicating a beginning flow separation in the shroud/suction-side corner of the flow channel. After considering possible causes for separation onset, it was concluded from measurement results that turbulence stabilization of the shroud/suction-side boundary layer, due to streamline curvature and system rotation effects, is probably of dominating influence.

3 Total enthalpy gradients normal to the meridional shroud contour are additionally strengthened when the channel flow separates near the shroud; then the turning to radial induces pronounced secondary vorticities. Consequently, the observed secondary flow pattern and its development along the flow passages is in qualitatively good agreement with theoretical predictions.

4 After separation onset there is a rapid growth of the wake area in the shroud/suction-side corner of the flow channel; this effect is presumably in strong interconnection with the strengthening secondary flow intensity. While secondary vortices peel the boundary layers off the channel walls—feeding low-energetic fluid into the wake—system rotation and curvature effects suppress turbulent mixing at the jet/wake shear layer; so the distorted flow is preserved and enhanced up to impeller discharge.

5 A loss analysis of the L2F data at impeller discharge indicates isentropic flow or only very small losses in the jet for the investigated case. The entropy generated within the impeller is mainly accumulated in the wake and along the channel walls. This loss pattern is probably produced by the prevailing secondary flows and maintained by the described flow mechanisms, due to Coriolis acceleration and meridional channel curvature.

These investigations were intended to deepen the insight into the complicated internal flow structure of high-speed centrifugal compressor impellers. The results should help to establish physically more relevant flow models and calculation methods—necessary preconditions for an ultimate design optimization of centrifugal compressor stages.

Acknowledgments

Present investigations at DFVLR were supported by a research contract from the Forschungsvereinigung Verbrennungskraftmaschinen, a joint research organization of German turbomachinery and combustion engine manufacturers. The author appreciated the assistance of his colleagues R. Schodl, K. J. Trültzsch, T. Klemmer, and W. Weimann in carrying out these research works.

References

1 Fischer, K., and Thoma, D., "Investigation of the Flow Conditions in a Centrifugal Pump," TRANS. ASME, Vol. 54, 1932, pp. 141–155.

2 Fujie, K., "Three-Dimensional Investigation of Flow in Centrifugal Impeller With Straight-Radial Blades," *Bulletin of JSME*, Vol. 1, No. 1, 1958, pp. 42–49.

3 Senoo, Y., Yamaguchi, M., and Nishi, M., "A Photografic Study of the Three-Dimensional Flow in a Radial Compressor," *Journal of Engineering for Power*, TRANS. ASME, Series A, July 1968, pp. 237–244.

4 Fowler, H. S., "Research on the Internal Aerodynamics of the Centrifugal Compressor," 11th Anglo-American Aeronautical Conference, London, Paper No. 19, Sept. 8–12, 1969, p. 15.

5 Howard, J. H. G., and Kittmer, C. W., "Measured Passage Velocities in a Radial Impeller With Shrouded and Unshrouded Configurations," ASME Paper No. 74-GT-66.

6 Mizuki, S., Ariga, I., and Watanabe, I., "A Study on the Flow Mechanism Within Centrifugal Impeller Channels," ASME Paper No. 75-GT-14.

7 Eckardt, D., "Applications of Dynamic Measurement Techniques for Unsteady Flow Investigations in Centrifugal Compressors," von Karman Institute, Lecture Series 66, *Advanced Radial Compressors*, Mar. 1974, p. 101.

8 Eckardt, D., "Instantaneous Measurements in the Jet-Wake Discharge Flow of a Centrifugal Compressor Impeller," *Journal of Engineering for Power*, TRANS. ASME, Series A, Vol. 97, No. 3, July 1975, pp. 337–346.

9 Schodl, R., "Laser Dual-Beam Method for Flow Measurements in Turbomachines," ASME Paper No. 74-GT-157.

10 Schodl, R., "A Dual-Focus-Velocimeter for Turbomachine Applications," von Karman Institute, Lecture Series 78, *Advanced Testing Techniques in Turbomachines*, Apr. 1975, p. 39.

11 Dean, R. C., Jr., "On the Unresolved Fluid Dynamics of the Centrifugal Compressor," *Advanced Centrifugal Compressors*, ASME, 1971, pp. 1–55.

12 Johnston, J. P., "The Effects of Rotation on Boundary Layers in Turbomachine Rotors," *Fluid Mechanics, Acoustics*

and Design of Turbomachinery, NASA SP-304, Part I, 1974, pp. 207–249.
13 Johnston, J. P., and Dean, R. C., Jr., "Losses in Vaneless Diffusers of Centrifugal Compressors and Pumps," *Journal of Engineering for Power*, TRANS. ASME, Series A, Vol. 88, No. 1, Jan. 1966, pp. 49–62.
14 Eckardt, D., "Investigations of the Disturbed Flow Pattern Within and at the Discharge from a High-Loaded Centrifugal Compressor Impeller," DLR-FB 75-39, 1975, p. 29.
15 Stanitz, J. D., "Two-Dimensional Compressible Flow in Turbomachines with Conic Flow Surfaces," NACA Rep. 935, 1949.
16 Stanitz, J. D., and Prian, V. D., "A Rapid Approximate Method for Determining Velocity Distribution on Impeller Blades of Centrifugal Compressors," NACA TN 2421, July 1951, p. 31.
17 Dean, R. C., Jr., "The Fluid Dynamic Design of Advanced Centrifugal Compressors," Creare, TN-153, Sept. 1972, p. 38.
18 Dean, R. C., Jr., Wright, D. D., and Runstadler, P. W., Jr., "Fluid Mechanics Analysis of High-Pressure-Ratio Centrifugal Compressor Data," USAAVLABS Technical Report 69-76, AD 872161, Feb. 1970, p. 565.
19 Kramer, J. J., and Stanitz, J. D., "A Note on Secondary Flow in Rotating Radial Channels," NACA Report 1179, 1954, p. 12.
20 Bradshaw, P., *Effects of Streamline Curvature on Turbulent Flow*, AGARDograph, No. 196, Aug. 1973, p. 130.
21 Eide, S. A., and Johnston, J. P., "Prediction of the Effects of Longitudinal Wall Curvature and System Rotation on Turbulent Boundary Layers," Thermosciences Division, Mechanical Engineering Department, Stanford University, Report PD-19, 1974, p. 101.
22 Moore, J., "A Wake and an Eddy in a Rotating Radial-Flow Passage," *Journal of Engineering for Power*, TRANS. ASME, Series A, Vol. 95, July 1973, pp. 205–219.
23 Rothe, P. H., and Johnston, J. P., "The Effect of System Rotation on Separation, Reattachment and Performance in Two-Dimensional Diffusers," Thermosciences Division, Mechanical Engineering Department, Stanford University, Report PD-17, 1975, p. 294.